PLOS ONE

RESEARCH ARTICLE

Monitoring Radiofrequency Ablation Using Ultrasound Envelope Statistics and Shear Wave Elastography in the Periablation Period: An *In Vitro* Feasibility Study

Po-Hsiang Tsui[1,2,3]*, Chiao-Yin Wang[1,4], Zhuhuang Zhou[5], Yung-Liang Wan[1,2,3]*

1 Department of Medical Imaging and Radiological Sciences, College of Medicine, Chang Gung University, Taoyuan, Taiwan, **2** Medical Imaging Research Center, Institute for Radiological Research, Chang Gung University and Chang Gung Memorial Hospital at Linkou, Taoyuan, Taiwan, **3** Department of Medical Imaging and Intervention, Chang Gung Memorial Hospital at Linkou, Taoyuan, Taiwan, **4** Graduate Institute of Clinical Medical Sciences, College of Medicine, Chang Gung University, Taoyuan, Taiwan, **5** College of Life Science and Bioengineering, Beijing University of Technology, Beijing, China

* tsuiph@mail.cgu.edu.tw (PHT); ylw0518@cgmh.org.tw (YLW)

Citation: Tsui P-H, Wang C-Y, Zhou Z, Wan Y-L (2016) Monitoring Radiofrequency Ablation Using Ultrasound Envelope Statistics and Shear Wave Elastography in the Periablation Period: An *In Vitro* Feasibility Study. PLoS ONE 11(9): e0162488. doi:10.1371/journal.pone.0162488

Editor: Chien-Wei Su, Taipei Veterans General Hospital, TAIWAN

Received: April 16, 2016

Accepted: August 2, 2016

Published: September 7, 2016

Data Availability Statement: All relevant data are within the paper and its Supporting Information files.

Funding: This work was supported by the Ministry of Science and Technology (Taiwan) under Grant No. MOST 103-2221-E-182-001-MY3 and the Chang Gung Memorial Hospital (Linkou, Taiwan) under Grant Nos. CMRPD1F0311, CMRPD1C0711, and CIRPD1E0022. The funders had no role in study design, data collection and analysis, decision to publish, or preparation of the manuscript.

Abstract

Radiofrequency ablation (RFA) is a minimally invasive method for treating tumors. Shear wave elastography (SWE) has been widely applied in evaluating tissue stiffness and final ablation size after RFA. However, the usefulness of periablation SWE imaging in assessing RFA remains unclear. Therefore, this study investigated the correlation between periablation SWE imaging and final ablation size. An *in vitro* porcine liver model was used for experimental validation ($n = 36$). During RFA with a power of 50 W, SWE images were collected using a clinical ultrasound system. To evaluate the effects of tissue temperature and gas bubbles during RFA, changes in the ablation temperature were recorded, and image echo patterns were measured using B-mode and ultrasound statistical parametric images. After RFA, the gross pathology of each tissue sample was compared with the region of change in the corresponding periablation SWE image. The experimental results showed that the tissue temperature at the ablation site varied between 70°C and 100°C. Hyperechoic regions and changes were observed in the echo amplitude distribution induced by gas bubbles. Under this condition, the confounding effects (including the temperature increase, tissue stiffness increase, and presence of gas bubbles) resulted in artifacts in the periablation SWE images, and the corresponding region correlated with the estimated final ablation size obtained from the gross pathology ($r = 0.8$). The findings confirm the feasibility of using periablation SWE imaging in assessing RFA.

Competing Interests: The authors have declared that no competing interests exist.

Introduction

Radiofrequency ablation (RFA) is a standard alternative treatment in oncologic treatments [1,2]. To guide the RF electrode to the target location of the tumor, surgeons typically use ultrasonography because it provides real-time feedback on the electrode location [3]. RFA-induced coagulation necrosis, which involves protein denaturation and tissue dehydration, increases tissue stiffness [4,5]. Several ultrasound elastography approaches, such as quasistatic elastography [6–10], real-time elastography [11], and acoustic radiation force impulse (ARFI) imaging [12–14], have been explored for RFA monitoring. However, most of these approaches cannot provide quantitative maps for tissue stiffness; therefore, shear wave elastography (SWE) was proposed [15,16].

In SWE, the shear wave velocity is measured to estimate the Young's modulus of the target tissue. Several previous studies have demonstrated the use of postablation SWE imaging in quantifying the stiffness of RFA-induced lesions *in vitro* and *in vivo* [17–21]. Crucial to ablation assessment is the spatial and temporal stability of tissue stiffness assessment; a recent study explored the use of SWE and ARFI imaging in monitoring the evolution of tissue stiffness at ablation sites during lesion formation in the periablation period [22]. Aside from tissue stiffness, the size of the ablation zone is the other critical factor in physicians' clinical evaluations of RFA efficiency. However, no previous study has revealed the relationship between periablation SWE and final ablation size.

The present study investigated the correlation between gross examination of the thermal lesion and the region of change in the periablation SWE image. The *in vitro* results indicated that the region of change in the SWE image obtained in the periablation period correlated with the gross pathology. The physical meanings and clinical value of periablation SWE imaging in RFA monitoring are discussed in this paper.

Materials and Methods

The experimental environment and measurement procedures are illustrated in Fig 1; the details are explained in the following paragraphs.

In vitro samples

An *in vitro* model based on porcine livers (obtained from the Donshi market at Linkou, Taiwan; WGS84 coordinates: 121.377680, 25.068978) was devised. Each liver sample was cut, placed in a case filled with a saline solution (0.9% NaCl), and compressed in the solution for degassing. Subsequently, each sample was placed in another case filled with a degassed saline solution. A gel phantom was created and applied to the bottom of the case to hold the samples and separate reflection echoes contributed at the bottom from backscattered signals received from the tissue. A metal board was attached to the wall of the case as a grounding pad for the RFA system.

Thermal lesions

The RFA system (Model VIVA RF generator, Starmed Co. Ltd., Goyang, Gyeonggi, South Korea) employed in the experiments comprised a Cool-tip RF electrode (Model 17-20V15-40, Starmed Co.), an RF generator, a peristaltic pump, cables, and other accessories. The active tip length (ATL) of the electrode can be adjusted to 0.5, 1.0, and 1.5 cm to produce thermal lesions of various sizes. The pump was used to deliver a constant flow of cold saline solution with a mixture of ice to the electrode tip to prevent the electrode from overheating, which would cause tissue carbonization. To measure the tissue temperature corresponding to the location of the electrode tip, a thermocouple was additionally attached to the electrode. Concurrently, the temperature of the electrode tip was automatically recorded by the RFA system. In the

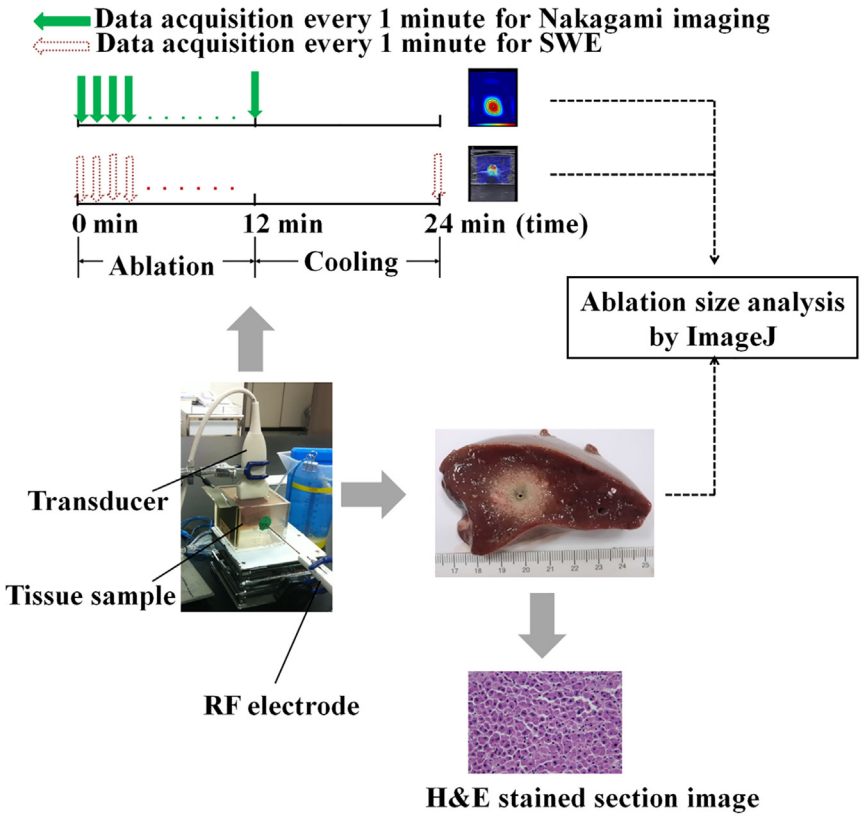

Fig 1. Experimental setting, design, and measurement procedures.

doi:10.1371/journal.pone.0162488.g001

experiments, the RF needle electrode was inserted into the liver sample through a small hole created in the case wall. The RFA system was subsequently turned on in clinical default mode (starting power: 50 W; treatment time: 12 min; operation frequency: 480 kHz) and automatically increased by 10 W/min until the RF pulse paused because of high tissue impedance. The system then generated a sequence of RF pulses as a function of time. At the endpoint of ablation (12 min), the RFA system automatically stopped.

B-mode and SWE imaging

During RFA, periablation B-mode and SWE images of each sample were acquired every minute by using a commercial SWE imaging system (Aixplorer, SuperSonic Imagine, France) equipped with an 8-MHz linear transducer. Postablation B-mode and SWE images were also obtained after the tissue sample was cooled for 24 min for measuring the Young's modulus by using a built-in circular region of interest (ROI) with a 5-mm diameter centered at the electrode location. All images were collected on a focal plane. For each ATL, independent experiments were conducted on six liver samples.

Nakagami imaging for bubble detection

Aside from the stiffness increase, RFA also induces gas bubbles in the ablation zone because ablation heating increases the tissue temperature close to the boiling point [7,23]. To examine whether the applied ablation power could induce bubbles during RFA, an additional six liver samples for each ATL (total $n = 36$) were ablated using the same protocol and monitored

through ultrasound Nakagami imaging, which is a parametric imaging technique based on the Nakagami parameter of the Nakagami distribution for modeling the echo amplitude distribution [24]. Studies have shown that RFA-induced bubbles significantly change the statistical distribution of backscattered signals, which can be visualized through ultrasound Nakagami imaging [25,26].

The detailed characteristics of the Nakagami imaging system employed in this study has been reported and validated in a previous study [26]. A clinical ultrasound scanner (Model 3000, Terason, Burlington, MA, USA) equipped with a 7.5-MHz linear transducer (Model 10L5, Terason) was connected to a computer; the software employed for real-time Nakagami imaging was developed in the C++ programming language. The algorithmic scheme for Nakagami imaging includes the following steps: (i) conduct frequency diversity by passing the raw image RF signals through two bandpass filters to produce two filtered data, and then compute the corresponding envelope images; (ii) apply the sliding window technique to the two envelope images to obtain their corresponding Nakagami images, which are summed and averaged to yield a compounding Nakagami image; and (iii) apply polynomial approximation to the compounding Nakagami image to visualize the region of change in the echo amplitude distribution (the area within the −6-dB contour was used as the estimate of the bubble region in this study).

Image analysis

The uses of size or shape parameters for evaluating the ablation zone depend on the type of active electrode. Ablation size is a frequently used parameter when needle-type electrodes are used [19,20,27,28]. The diameter, length, and shape are considered when RFA is performed using an umbrella-shaped electrode [29,30]. Considering the experimental design in the present study, ablation size was used to evaluate the ablation zone.

Each periablation SWE image acquired during RFA was analyzed using the software ImageJ (a public domain image processing program developed by the National Institutes of Health) to quantitatively measure the region of change in the shading of the SWE image, denoted by S_{SWE} with mm^2 as the unit. The steps for estimating S_{SWE} by using ImageJ are illustrated and explained in Fig 2. To investigate the behaviors of periablation SWE during RFA, we calculated S_{SWE} as a function of ablation time. Concurrently, gas bubble generation in the ablation zone is continual during RFA because of heating and the temperature approaching the boiling point. The appearance of gas bubbles can be used to assess the heated region [23], which correlates with the ablated zone [25]. To collect sufficient backscattering information on the bubbles to improve ablation zone visualization, the average of S_{SWE} acquired at the 1st, 2nd, . . ., 12th min (i.e., the temporal compounding of images [26]) was also calculated as an overall evaluation of periablation SWE ($\overline{S_{SWE}^{1-12\text{min}}}$). Moreover, the size of the area with changes in the backscattered statistics, denoted by $S_{Nakagami}$ with mm^2 as the unit, serving as a function of ablation time, as well as the average of $S_{Nakagami}$ acquired from the 1st to 12th min ($\overline{S_{Nakagami}^{1-12\text{min}}}$), were calculated to evaluate the behavior of gas bubbles during RFA. The value of $S_{Nakagami}$ was calculated online through the Nakagami imaging system [26]. Based on the technique of temporal compounding of images, the total measurement time for monitoring one sample to be ablated was determined by the treatment duration of RFA (i.e., 12 min).

Gross and pathological examinations

After image acquisition, the samples were cut along the ultrasound imaging plane and photographed for gross examination. The photographs (i.e., tissue section images), analyzed using ImageJ, served as the ground truths for measuring the size of the ablation zones. The procedure for processing the tissue section images is shown in Fig 2. To further examine the change in cell

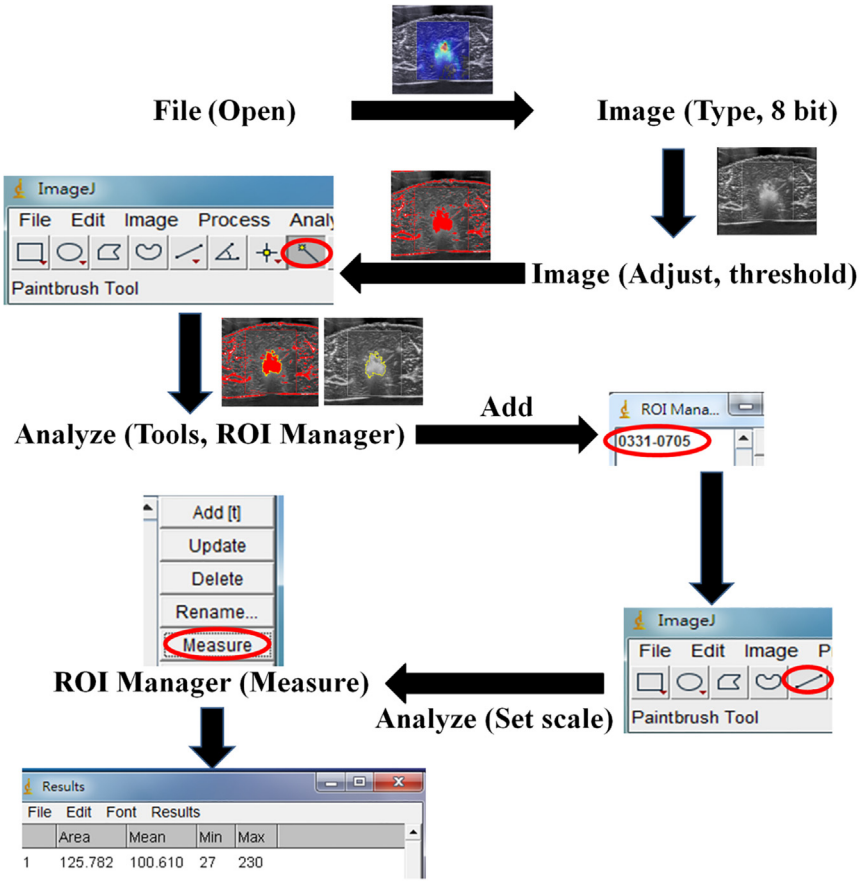

Fig 2. Illustration of the steps for estimating the region of change in the shading of the SWE image through ImageJ. First, the JPEG image file was read and converted into an 8-bit grayscale image. The threshold value—determined by averaging the gray scales in the ROI (approximately 3 × 3 mm) in the unablated zone—was then used to highlight the ablation zone, which was then contoured using the ROI manager in ImageJ to measure the ablation size according to the calibrated pixel scale.

doi:10.1371/journal.pone.0162488.g002

morphology caused by RFA, each tissue sample was fixed in 10% neutral buffered formalin, embedded in paraffin, and sliced into 4-μm-thick sections for histological analysis, in which hematoxylin and eosin (H&E) staining was employed. An experienced pathologist determined whether tissue necrosis was induced through RFA.

Data comparison

The experimental results obtained using different ATLs were compared to calculate the p value by using an independent Student's t test. Statistical significance was defined as $p < 0.05$. The measurements obtained from the SWE and Nakagami images were compared with the gross pathology to calculate the correlation coefficient r by using a linear curve fitting with the equation form of $y = y_0 + ax$. Statistical analysis was performed using the software SigmaPlot (Version 9.0, Systat Software, Inc., CA, USA).

Results

Fig 3(a) and 3(b) present typical temperature curves as a function of the ablation time measured from a liver sample and the electrode tip, respectively. During RFA, the tissue

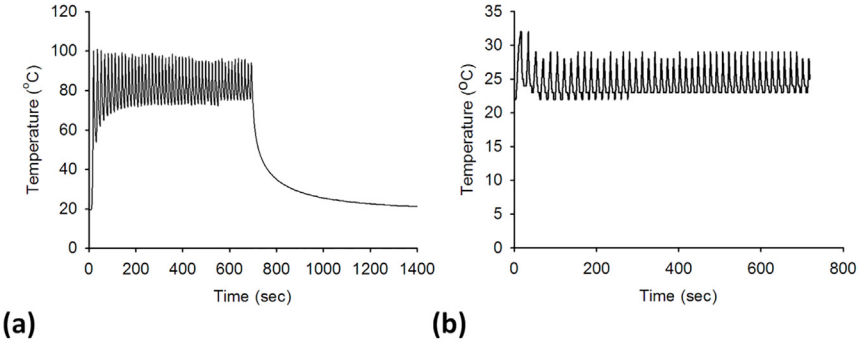

Fig 3. (a) A typical temperature curve as a function of the ablation time, measured using the thermocouple; (b) the temperature curve as a function of the ablation time, recorded from the electrode tip.

doi:10.1371/journal.pone.0162488.g003

temperature varied between 70°C and 100°C. When the RFA system stopped, the tissue temperature rapidly decreased to the initial value. The temperature of the electrode tip varied between 20°C and 30°C during RFA. Fig 4(a)–4(c) show the postablation SWE images of liver samples ablated using ATLs from 0.5 to 1.5 cm. The Young's moduli of the ablated liver samples varied between approximately 50 and 60 kPa, and were considerably higher than those observed before RFA ($p < 0.05$), as shown in Fig 4(d).

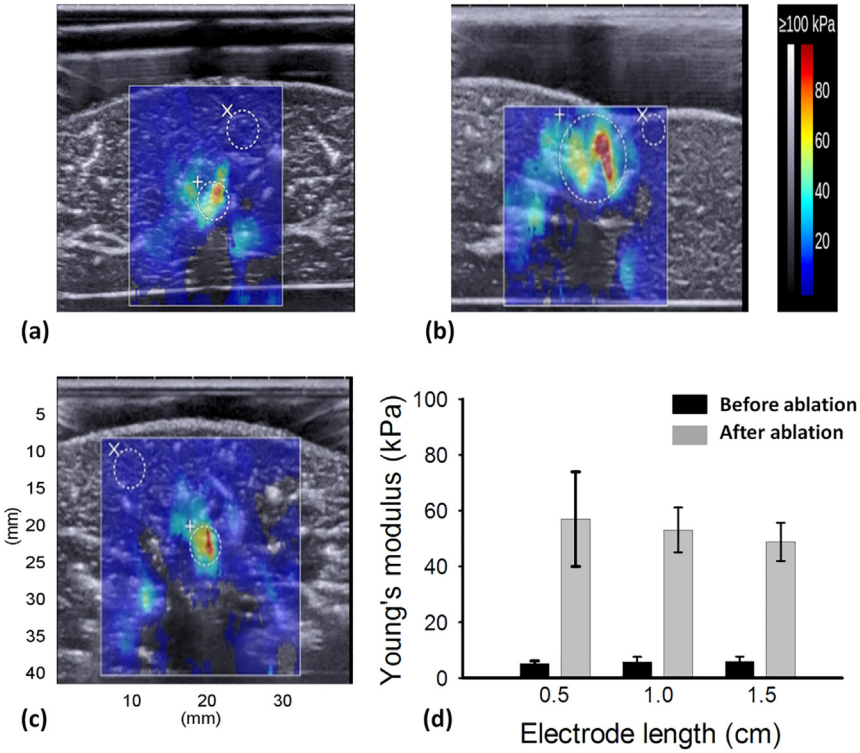

Fig 4. Postablated SWE images of liver samples ablated using ATLs of (a) 0.5 cm, (b) 1.0 cm, and (c) 1.5 cm. (d) Young's moduli of porcine livers before and after RFA.

doi:10.1371/journal.pone.0162488.g004

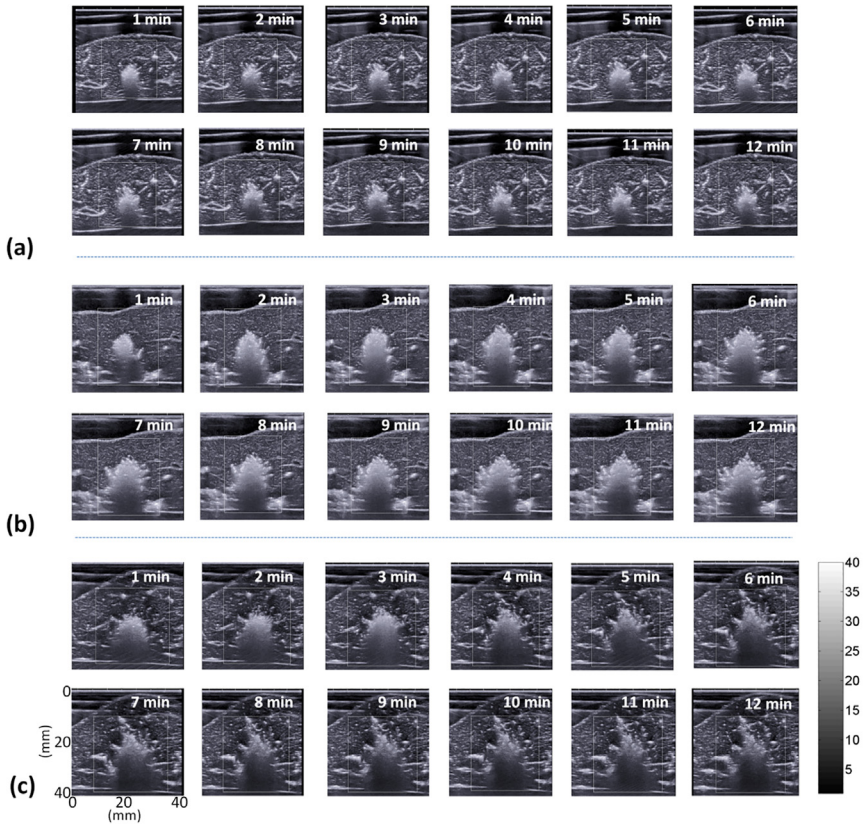

Fig 5. Ultrasound B-mode images acquired at various time points during RFA by using ATLs of (a) 0.5 cm, (b) 1.0 cm, and (c) 1.5 cm.

doi:10.1371/journal.pone.0162488.g005

Fig 5 shows the periablation B-mode images obtained using various ATLs. Hyperechoic regions were found in the ablation zone. Regions of change in the backscattered statistics (shown with green to red shading) were also detected in the ablation zone in the periablation Nakagami images, as shown in Fig 6. Periablation SWE images also showed changes in image shading during RFA, as indicated in Fig 7. To indicate the correlation between the gross examinations and visualized regions of change in the periablation images, the results of the quantitative analysis are given in Figs 8 and 9. For each ATL, both S_{SWE} and $S_{Nakagami}$ exhibited a slight increase with the ablation time, as shown in Fig 8. The $\overline{S_{SWE}^{1-12\text{min}}}$ value increased from 63.87 ± 20.48 mm^2 to 190.43 ± 41.45 mm^2 as the ATL increased from 0.5 to 1.5 cm ($p < 0.05$ between each ATL). In this range of ATLs, the $\overline{S_{Nakagami}^{1-12\text{min}}}$ value increased from 51.75 ± 7.13 mm^2 to 196.42 ± 67.81 mm^2 ($p < 0.05$ between each ATL), as shown in Fig 9(a) and 9(b). In particular, Fig 9(c) and 9(d) show that $\overline{S_{SWE}^{1-12\text{min}}}$ and $\overline{S_{Nakagami}^{1-12\text{min}}}$ were closely correlated with the final ablation size ($r = 0.8$ and 0.85 for the SWE and Nakagami images, respectively).

Discussion

Research contributions

First, we summarize the significances and findings of this study and then discuss the details later. Note that the relationship between $\overline{S_{Nakagami}^{1-12\text{min}}}$ and the final ablation size was validated in a previous study [26]. However, the dependency of $\overline{S_{SWE}^{1-12\text{min}}}$ on the final ablation size is a new

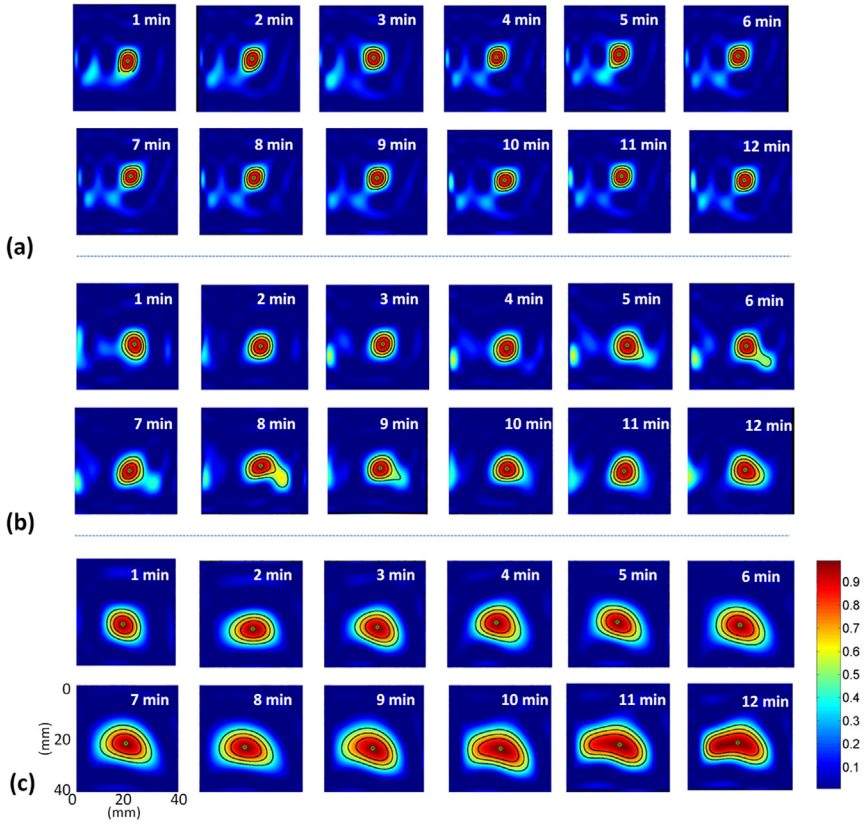

Fig 6. Ultrasound Nakagami images acquired at various time points during RFA by using ATLs of (a) 0.5 cm, (b) 1.0 cm, and (c) 1.5 cm.

doi:10.1371/journal.pone.0162488.g006

finding. Previously, postablation SWE has been widely explored in evaluating tissue stiffness and ablation size. However, no previous study has reported the usefulness of periablation SWE imaging in estimating ablation size. The present study is the first to conduct *in vitro* experiments to clarify the role of periablation SWE imaging in monitoring RFA. The results show that $\overline{S_{SWE}^{1-12\text{min}}}$ depends on the gross pathology, indicating that using periablation SWE imaging in assessing RFA is feasible.

Peri- and postablation SWE in stiffness assessment

Clinically successful tumor ablation therapy requires that cells are completely destroyed by substantial thermal effects. The *in vitro* model and experimental setup used in this study provide a simulation of RFA-induced tissue necrosis. As indicated in Fig 3, the tissue temperature at the ablation site varied between 70°C and 100°C. A temperature of approximately 100°C for a 12-min ablation results in a sufficient thermal dose to completely destroy cells.

Tissue necrosis involving protein denaturation and tissue dehydration increases tissue stiffness. Clinically, monitoring the final stiffness of the ablation zone is essential to guarantee the treatment efficacy of RFA and mitigate complications. SWE is currently a state-of-the-art ultrasound tool used for detecting tissue stiffness following RFA. The results in Fig 4 show the use of SWE in stiffness assessment. Previous studies have reported the performance of SWE in monitoring RFA [17–21]. Although different models and RFA systems and parameters have

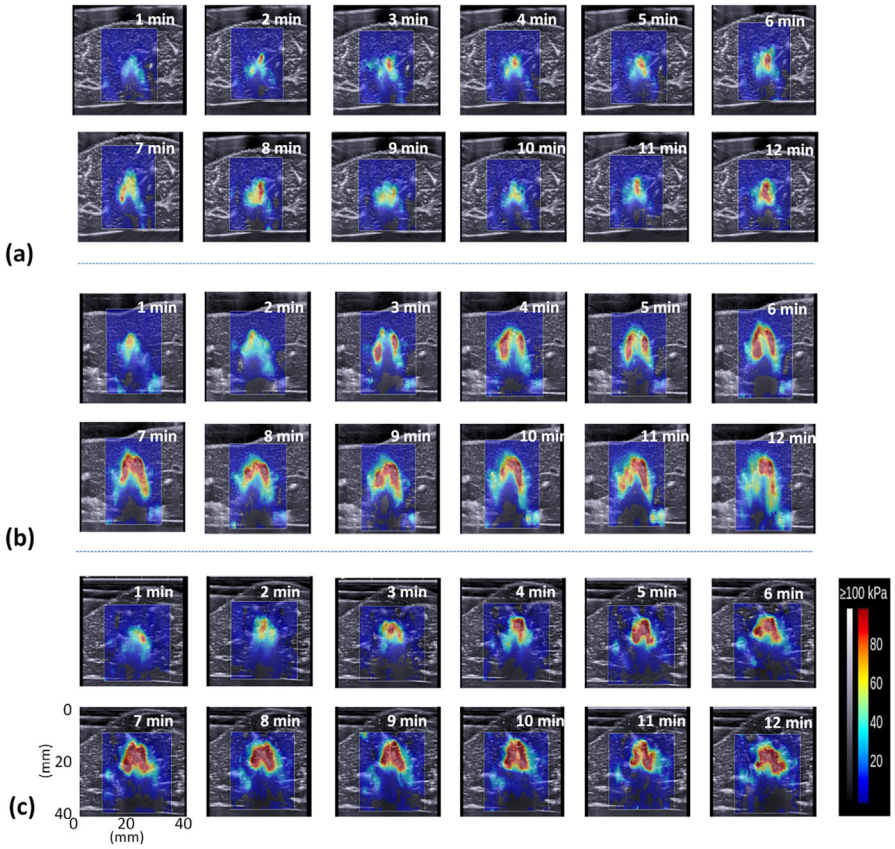

Fig 7. SWE images acquired at various time points during RFA by using ATLs of (a) 0.5 cm, (b) 1.0 cm, and (c) 1.5 cm. These images correspond to the Nakagami images shown in Fig 6.

doi:10.1371/journal.pone.0162488.g007

been used in these studies, they have been consistent in their conclusion that final tissue stiffness and ablation size can be effectively assessed using postablation SWE images obtained after tissue cooling. However, under high-power RFA, we noted that the contour of the ablation zone was not clearly visualized in the postablation SWE images, as shown in Fig 4. This may be attributable to the shear wave attenuation. The attenuation of a shear wave in tissues is determined according to the density, shear elasticity, and shear viscosity of the tissue [31]. Thermal ablation increases the shear elasticity and viscosity [32], which continue to increase at temperatures higher than 70°C because tissues lose most of their water content above this temperature [33]. The aforementioned conditions may result in significant shear wave attenuation, which reduces the signal-to-noise ratio of the shear wave signal, thereby influencing the formation of the postablation SWE image and the corresponding image quality.

Regarding the value of periablation SWE images in monitoring RFA, a recent study explored the use of periablation SWE and ARFI imaging for describing changes in tissue stiffness during RFA [22]. That study found that through the SWE and ARFI methods, an immediate increase was detected in tissue stiffness during RFA, suggesting that a consistent stiffness assessment is possible 2 min after and for at least 30 min following ablation. However, the relationship between periablation SWE imaging and the final ablation size was not clarified; furthermore, the physical meanings of the periablation SWE images remain unclear. In our opinion, the physical meanings of periablation SWE imaging only partially correlate with the tissue stiffness because several effects occur during RFA, which are discussed as follows.

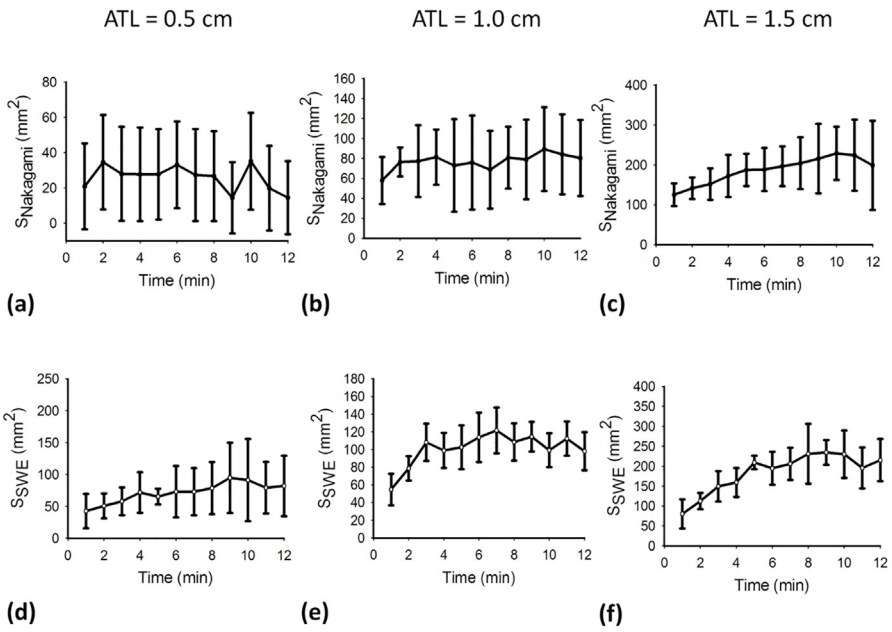

Fig 8. Values of (a)–(c) the size of the area with changes in the backscattered statistics and (d)–(f) the size of the region with changes in the shading of the SWE image as a function of the ablation time, obtained using various ATLs.

doi:10.1371/journal.pone.0162488.g008

Physical effects and mechanisms of periablation SWE in evaluating ablation size

First, significant thermal effects induced by RFA may affect the biomechanical properties of tissues. For instance, the shear modulus of the liver tissue was nearly constant during heating, increasing exponentially once the tissue temperature exceeded 45°C [34]. In other words, estimation of the tissue stiffness in the periablation period may be affected by the temperature effect. Second, under high-temperature ablation, we observed the image pattern of gas bubbles (i.e., the hyperechoic region) in the B-mode image, as illustrated in Fig 5. Concurrently, a change in the echo amplitude distribution caused by gas bubbles was also detected through Nakagami imaging, as shown in Fig 6. Note that the effects of water vaporization and gas bubble formation during RFA affect SWE imaging [19]. Gas bubbles in aqueous soft tissues may generate a bubble-based radiation force when sonicated by an ultrasound beam [35,36]. The radiation force generated by the bubbles may interact with that of the push beams used for SWE imaging, thereby affecting the formation of the periablation SWE image. Third, to create an SWE image, the speckle motion resulting from shear wave propagation is typically computed using cross-correlation-based techniques on successive images acquired by ultrafast imaging for shear wave velocity estimation. During RFA, new bubbles form, and old bubbles may dissipate (collapse) as the tissue temperature increases [7]. The formation and collapse of bubbles during RFA cause the waveforms of ultrasound signals to vary with time, resulting in computational errors in the cross-correlation analysis between the two acquired images, which results in SWE image artifacts.

According to this discussion, changes in the periablation SWE images obtained during RFA may be attributable to confounding effects including the temperature increase, stiffness (including elasticity and viscosity [32,33]) increase, and bubble-related artifacts. Therefore, the data for periablation SWE images acquired during RFA no longer represent the tissue stiffness. As mentioned, a previous study reported a correlation between the formation of bubbles and

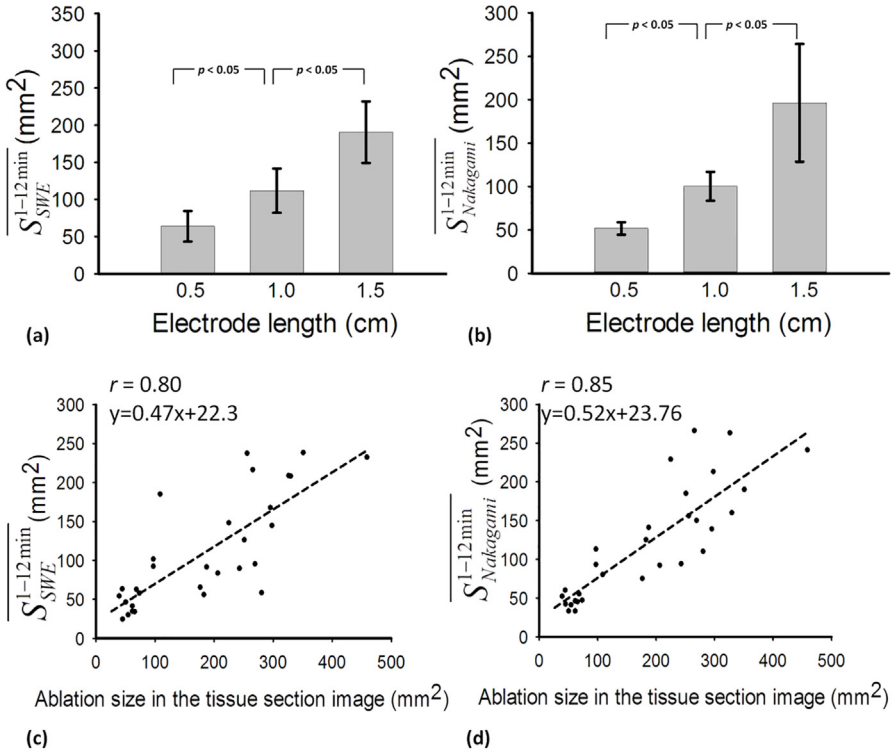

Fig 9. Regions with changes in the shading of (a) SWE and (b) Nakagami images taken during RFA with various ATLs. The ablation sizes obtained from the tissue section images are compared with those obtained from (c) SWE and (d) Nakagami images.

doi:10.1371/journal.pone.0162488.g009

the areas being treated by RFA [23]. In this condition, the confounding effects (particularly for bubble-related artifacts) become key factors causing periablation SWE imaging to correlate with the final ablation size, although the confounding effects result in ambiguity of the physical meanings in the periablation SWE images.

Future work

First, *in vivo* environments were not considered in the employed model. Blood perfusion reduces the ablation temperature, resulting in different ablation volumes, depending on the probe location (e.g., the proximity to a large vessel) [37]; the effect of perfusion on periablation SWE imaging should be further explored clinically. Second, the formation, distribution, and dynamics of gas bubbles occurring during RFA represent complex problems, which result in heterogeneity of periablation SWE images (as shown in Fig 7), and may depend on the properties of the target tissues. The applicability of periablation SWE imaging to various types of tissues is also a crucial research topic. Third, in clinical nodules, the hyperechoic area caused by gas bubbles may disappear and gradually change into the hyperechoic rim around the nodule within 5–15 min after RFA [38]. The hyperechoic rim is related to the necrotic area, although it may be inaccurate [38]. Combining the bubble-related artifacts in periablation images and the hyperechoic rim feature in postablation images may benefit evaluations of clinical RFA.

Conclusion

In this study, experiments were conducted on an *in vitro* model to explore the correlation between periablation SWE imaging and gross examination of thermal lesions induced by high-temperature RFA. The results reveal that the region of change in SWE images obtained in the periablation period correlates with the gross pathology. Changes in the periablation SWE images may be attributable to the confounding effects based on the temperature increase, stiffness increase, and bubble-related artifacts. The findings of this study confirm the feasibility of using periablation SWE imaging in assessing RFA.

Supporting Information

S1 Code. Source codes for imaging and processing.
(RAR)

S1 Data. Data for the ablation sizes obtained from SWE, Nakagami, and tissue section images.
(RAR)

Author Contributions

Conceptualization: PHT.

Data curation: CYW.

Formal analysis: CYW ZZ.

Funding acquisition: PHT.

Investigation: CYW.

Methodology: PHT CYW ZZ.

Project administration: PHT.

Resources: YLW.

Software: PHT ZZ.

Supervision: PHT.

Validation: CYW.

Visualization: CYW.

Writing – original draft: PHT.

Writing – review & editing: PHT.

References

1. Bruix J, Sherman M (2011) Management of hepatocellular carcinoma: an update. Hepatology 53: 1020–1022. doi: 10.1002/hep.24199 PMID: 21374666
2. Shah DR, Green S, Elliot A, McGahan JP, Khatri VP (2013) Current oncologic applications of radiofrequency ablation therapies. World J Gastrointest Oncol 5: 71–80. doi: 10.4251/wjgo.v5.i4.71 PMID: 23671734
3. Machi J, Uchida S, Sumida K, Limm WM, Hundahl SA, Oishi AJ, et al. (2001) Ultrasound-guided radiofrequency thermal ablation of liver tumors: percutaneous, laparoscopic, and open surgical approaches. J Gastrointest Surg 5: 477–489. PMID: 11985998

4. Zhou Z, Wu W, Wu S, Xia J, Wang CY, Yang C, et al. (2014) A survey of ultrasound elastography approaches to percutaneous ablation monitoring. Proc Inst Mech Eng H 228: 1069–1082. doi: 10.1177/0954411914554438 PMID: 25332155
5. Brosses ES, Pernot M, Tanter M (2011) The link between tissue elasticity and thermal dose in vivo. Phys Med Biol 21: 7755–7765.
6. Varghese T, Techavipoo U, Liu W, Zagzebski JA, Chen Q, Frank G, et al. (2003) Elastographic measurement of the area and volume of thermal lesions resulting from radiofrequency ablation: pathologic correlation. AJR Am J Roentgenol 181: 701–707. PMID: 12933463
7. Varghese T, Techavipoo U, Zagzebski JA, Lee FT (2004) Impact of gas bubbles generated during interstitial ablation on elastographic depiction of in vitro thermal lesions. J Ultrasound Med 23: 535–544. PMID: 15098873
8. Pareek G, Wilkinson ER, Bharat S, Varghese T, Laeseke PF, Lee FTJ, et al. (2006) Elastographic measurements of in-vivo radiofrequency ablation lesions of the kidney. J Endourol 20: 959–964. PMID: 17144871
9. Rivaz H, Fleming I, Assumpcao L, Fichtinger G, Hamper U, Choti M, et al. (2008) Ablation monitoring with elastography: 2D in-vivo and 3D ex-vivo studies. Med Image Comput Comput Assist Interv 11: 458–466. PMID: 18982637
10. Vledder MGV, Boctor EM, Assumpcao LR, Rivaz H, Foroughi P, Hager GD, et al. (2010) Intra-operative ultrasound elasticity imaging for monitoring of hepatic tumour thermal ablation. HPB (Oxford) 12: 717–723.
11. Zhang M, Castaneda B, Christensen J, Saad WE, Bylund K, Hoyt K, et al. (2008) Real-time sonoelastography of hepatic thermal lesions in a swine model. Med Phys 35: 4132–4141. PMID: 18841866
12. Fahey BJ, Nightingale KR, Stutz DL, Trahey GE (2004) Acoustic radiation force impulse imaging of thermally- and chemically-induced lesions in soft tissues: preliminary ex vivo results. Ultrasound Med. Biol. 30: 321–328. PMID: 15063514
13. Fahey BJ, Nelson RC, Hsu SJ, Bradway DP, Trahey GE (2008) In vivo guidance and assessment of liver radio-frequency ablation with acoustic radiation force elastography. Ultrasound Med. Biol. 34: 1590–1603. doi: 10.1016/j.ultrasmedbio.2008.03.006 PMID: 18471954
14. Kwon HJ, Kang MJ, Cho JH, Oh JY, Nam KJ, Han SY, et al. (2011) Acoustic radiation force impulse elastography for hepatocellular carcinoma-associated radiofrequency ablation. World J Gastroenterol 17: 1874–1878. doi: 10.3748/wjg.v17.i14.1874 PMID: 21528062
15. Bercoff J, Tanter M, Fink M (2004) Supersonic shear imaging: a new technique for soft tissue elasticity mapping. IEEE Trans. Ultrason. Ferroelec. Freq. Contr. 51: 396–409.
16. Athanasiou A, Tardivon A, Tanter M, Sigal-Zafrani B, Bercoff J, Deffieux T, et al. (2010) Breast lesions: quantitative elastography with supersonic shear imaging—preliminary results. Radiology 256: 297–303. doi: 10.1148/radiol.10090385 PMID: 20505064
17. Pernot M, Mace E, Dubois R, Couade M, Fink M, Tanter M (2009) Mapping myocardial elasticity changes after RF-ablation using supersonic shear imaging. Comput Cardiol 36: 793–796.
18. Hollender P, Rosenzweig S, Eyerly S, Wolf P, Trahey G (2013) Three-dimensional fusion of Shear Wave Imaging and electro-anatomical mapping for intracardiac radiofrequency ablation monitoring. IEEE Ultrason. Symp. Proc. 1: 108–111.
19. Mariani A, Kwiecinski W, Pernot M, Balvay D, Tanter M, Clement O, et al. (2014) Real time shear waves elastography monitoring of thermal ablation: in vivo evaluation in pig livers. J Surg Res 188: 37–43. doi: 10.1016/j.jss.2013.12.024 PMID: 24485877
20. Sugimoto K, Oshiro H, Ogawa S, Honjo M, Hara T, Moriyasu F (2014) Radiologic-pathologic correlation of three-dimensional shear-wave elastographic findings in assessing the liver ablation volume after radiofrequency ablation. World J Gastroenterol 20: 11850–11855. doi: 10.3748/wjg.v20.i33.11850 PMID: 25206291
21. Kwiecinski W, Provost J, Dubois R, Sacher F, Haissaguerre M, Legros M, et al. (2014) Quantitative evaluation of atrial radio frequency ablation using intracardiac shear-wave elastography. Med Phys 41: 112901. doi: 10.1118/1.4896820 PMID: 25370668
22. Eyerly SA, Vejdani-Jahromi M, Dumont DM, Trahey GE, Wolf PD (2015) The evolution of tissue stiffness at radiofrequency ablation sites during lesion formation and in the peri-ablation period. J Cardiovasc Electrophysiol 26: 1009–1018.
23. Winkler I, Adam D (2011) Monitoring radio-frequency thermal ablation with ultrasound by low frequency acoustic emissions—in vitro and in vivo study. Ultrasound Med. Biol. 37: 755–767. doi: 10.1016/j.ultrasmedbio.2010.11.008 PMID: 21497718

24. Fang J, Chen CK, Peng JY, Hsu CH, Jeng YM, Lee YH, et al. (2015) Changes in backscattered ultrasonic envelope statistics as a function of thrombus age: an in vitro study. Ultrasound Med. Biol. 41: 498–508. doi: 10.1016/j.ultrasmedbio.2014.09.024 PMID: 25542488

25. Wang CY, Geng X, Yeh TS, Liu HL, Tsui PH (2013) Monitoring radiofrequency ablation with ultrasound Nakagami imaging. Med Phys 40: 072901. doi: 10.1118/1.4808115 PMID: 23822452

26. Zhou Z, Wu S, Wang CY, Ma HY, Lin CC, Tsui PH (2015) Monitoring radiofrequency ablation using real-time ultrasound Nakagami imaging combined with frequency and temporal compounding techniques. PLoS One 10: e0118030. doi: 10.1371/journal.pone.0118030 PMID: 25658424

27. Liu W, Techavipoo U, Varghese T, Zagzebski JA, Chen Q, Lee FTJ (2004) Elastographic versus x-ray CT imaging of radio frequency ablation coagulations: an in vitro study. Med Phys 31: 1322–1332. PMID: 15259635

28. Wright AS, Sampson LA, Warner TF, Mahvi DM, Lee FTJ (2005) Radiofrequency versus microwave ablation in a hepatic porcine model. Radiology 236: 132–139. PMID: 15987969

29. Pereira PL, Trubenbach J, Schenk M, Subke J, Kroeber S, Schaefer I, et al. (2004) Radiofrequency ablation: in vivo comparison of four commercially available devices in pig livers. Radiology 232: 482–490. PMID: 15286318

30. Appelbaum L, Sosna J, Pearson R, Perez S, Nissenbaum Y, Mertyna P, et al. (2010) Algorithm optimization for multitined radiofrequency ablation: comparative study in ex vivo and in vivo bovine liver. Radiology 254: 430–440. doi: 10.1148/radiol.09090207 PMID: 20093515

31. Urban MW, Greenleaf JF (2009) A Kramers-Kronig-based quality factor for shear wave propagation in soft tissue. Phys Med Biol 54: 5919–5933. doi: 10.1088/0031-9155/54/19/017 PMID: 19759409

32. Shahmirzadi D, Hou GY, Chen J, Konofagou EE (2014) Ex Vivo characterization of canine liver tissue viscoelasticity after high-intensity focused ultrasound ablation. Ultrasound Med. Biol. 40: 341–350. doi: 10.1016/j.ultrasmedbio.2013.09.016 PMID: 24315395

33. Kiss MZ, Daniels MJ, Varghese T (2009) Investigation of temperature-dependent viscoelastic properties of thermal lesions in ex vivo animal liver tissue. J Biomech 42: 959–966. doi: 10.1016/j.jbiomech.2009.03.002 PMID: 19362313

34. Brosses ES-d, Gennisson JL, Pernot M, Fink M, Tanter M (2010) Temperature dependence of the shear modulus of soft tissues assessed by ultrasound. Phys Med Biol 55: 1701–1718. doi: 10.1088/0031-9155/55/6/011 PMID: 20197599

35. Gateau J, Pernot M, Tanter M, Fink M (2009) Imaging the effect of acoustically induced cavitation bubbles on the generation of shear-waves by ultrasonic radiation force. Proceedings of the 7th International Symposium on Cavitation 1: 16–20.

36. Erpelding TN, Hollman KW, O'Donnell M (2005) Bubble-based acoustic radiation force elasticity imaging. IEEE Trans. Ultrason. Ferroelec. Freq. Contr. 52: 971–979.

37. Ritz JP, Lehmann KS, Isbert C, Reissfelder C, Albrecht T, Stein T, et al. (2006) In-vivo evaluation of a novel bipolar radiofrequency device for interstitial thermotherapy of liver tumors during normal and interrupted hepatic perfusion. J Surg Res 133: 176–184. PMID: 16360176

38. Uehara T, Hirooka M, Kisaka Y, Abe M, Hiasa Y, Onji M (2009) Usefulness of the hyperechoic rim for assessing the therapeutic efficacy of radiofrequency ablation in hepatocellular carcinoma patients. Hepatol Res 39: 954–962. doi: 10.1111/j.1872-034X.2009.00537.x PMID: 19624769